Journal of Materials Chemistry A

PAPER

View Article Online
View Journal | View Issue



Cite this: J. Mater. Chem. A, 2019, 7, 20369

# Blade coated P3HT:non-fullerene acceptor solar cells: a high-throughput parameter study with a focus on up-scalability†

Enrique Pascual-San-José,[ab] Xabier Rodríguez-Martínez,[a] Rana Adel-Abdelaleim,[ab] Marco Stella,[b] Eugenia Martínez-Ferrero[b] and Mariano Campoy-Quiles*[a]

Combining non-fullerene acceptors (NFAs) with novel low band gap polymers has led to very promising performances. However, research on donors that can reduce the performance–cost gap, such as poly(3-hexylthiophene) (P3HT), can play an instrumental role in the upscaling of this technology. In this paper, we have analysed the influence of several processing parameters on the performance of solar cells based on P3HT:NFA binaries deposited by blade coating. The investigated NFAs include molecules with variations in the side chains and end-capping groups. More precisely, we have looked at devices based on P3HT blended with five NFAs, namely ITIC, ITIC-M, O-IDTBR, EH-IDTBR, and O-IDFBR, and employed $PC_{60}BM$ and ICBA as reference acceptors. More than one thousand doctor-bladed P3HT:NFA samples were manufactured using high throughput techniques using gradients of both thickness and annealing temperature. The combined data for all samples were employed to perform a parameter sensitivity study in order to identify the most influential parameters for P3HT based devices. For all material combinations, we have found that blade coated solar cells fabricated from chlorobenzene/dichlorobenzene mixtures outperform those based on chlorobenzene. For the most promising binary (*i.e.* P3HT:O-IDTBR), we have investigated in more depth the effects resulting from the choice of solvent, as well as casting temperature and post-deposition thermal annealing. Devices with power conversion efficiencies greater than 5% were obtained regardless of the casting temperature and for a relatively wide thickness range (80–250 nm). Finally, we have shown that encapsulated devices exhibit a stable performance for more than 3000 h and that degradation progresses faster in thicker devices. O-IDTBR has been identified to play a major role in the device degradation.

Received 8th July 2019
Accepted 3rd August 2019

DOI: 10.1039/c9ta07361b

rsc.li/materials-a



## Introduction

Solution-processed organic photovoltaics (OPVs) have attracted tremendous interest from both academy and industry. The synthesis of new and efficient types of acceptor materials including small molecule non-fullerene acceptors (NFAs)[1,2] and polymeric acceptors (all-polymer solar cells)[3–5] has opened up a new promising era. Currently, NFA-based OPVs have taken the technology over the 15% efficiency milestone[6,7] and up to 17.3% in the tandem configuration.[8] Some of the attractive traits of NFAs include tunable energy levels, absorption enhancement and lower synthetic cost compared to fullerenes. In addition, the ease modification of NFA absorption allows tuning the aesthetic appearance of the solar cell and facilitates integration into buildings.[9] The reported record photovoltaic devices are based on photoactive layers containing NFAs and low band-gap polymers.[7] Despite the outstanding performance of these low band-gap polymer:NFA systems, they have two main up-scaling challenges: long-term stability and synthetic scalability. In fact, the production of these polymer materials requires several synthetic steps, which makes a significant reduction of their embodied production cost unlikely.[10]

Poly(3-hexylthiophene), P3HT, is one of the most studied polymers in the OPV field.[11] P3HT has very simple and optimized synthetic steps,[12] a fact which currently allows purchasing kilograms of this polymer at a moderate cost.[13–15] Historically, P3HT has been blended with fullerene acceptors, such as [6,6]-phenyl-$C_{60}$-butyric acid methyl ester ($PC_{60}BM$) or indene-$C_{60}$ bisadduct (ICBA), yielding power conversion efficiencies (PCEs) of 4.5% or 6.5%, respectively, for spin-coated devices.[16,17] Furthermore, P3HT:fullerene systems have been used in the fabrication of the first generation of OPV modules.[18] With the appearance of high performing low-bandgap

[a]Institut de Ciència de Materials de Barcelona (ICMAB-CSIC), Campus de la UAB, Bellaterra, Barcelona, 08193, Spain. E-mail: mcampoy@icmab.es
[b]EURECAT, Centre Tecnológic de Catalunya, Parc Científic i de la Innovació TecnoCampus, Av. de Ernest Lluch, 36, Mataró, Barcelona, 08302, Spain

† Electronic supplementary information (ESI) available. See DOI: 10.1039/c9ta07361b

polymers, research interest has gradually shifted away from P3HT. In 2016, however, Holliday *et al.* for the first time synthesised an NFA that when blended with P3HT exceeded 6.3% efficiency in spin-coated devices.[19] The acceptor molecule included an indacenodithiophene core with benzothiadiazole and rhodanine flanking groups ((5*Z*,5′*Z*)-5,5′-((((4,4,9,9-tetraoctyl-4,9-dihydro-*s*-indaceno[1,2-*b*:5,6-*b*′]dithiophene-2,7-diyl) bis(benzo[*c*][1,2,5]thiadiazole-7,4-diyl))bis(methanylylidene)) bis(3-ethyl-2-thioxothiazolidin-4-one)) (O-IDTBR). This molecule showed a significantly enhanced optical absorption compared to fullerenes together with good device stability in air. Since then, O-IDTBR has been intensively studied in terms of carrier transport and recombination,[20–22] theoretical solubility by means of machine learning approaches[23] and the influence of P3HT molecular weight on the OPV performance.[24] The broad absorption of the P3HT:O-IDTBR system also made it attractive as a photodetector active layer, being sensitive to light from the visible to the near infrared regions.[25] Additionally, Baran *et al.* showed that introducing a third component, namely O-IDFBR, into the P3HT:O-IDTBR blend increased the PCE up to 7.7%.[26] Interestingly, O-IDTBR also demonstrated great performance when blended with other wide band-gap polymers (PvBDTTAZ and PBDTTT-EFT), exceeding 11% PCE.[26,27]

There are few reports on P3HT blended with other planar NFAs beyond the IDTBR and IDFBR families. For instance, a benzotriazole molecule mixed with P3HT extended the $V_{oc}$ to values over 1 V, yielding an efficiency of 4.5%.[28] Moreover, other P3HT blends based on benzotriazole with octyl side chains led to 6% efficiency.[29] On the other hand, 3,9-bis(2-methylene-(3-(1,1-dicyanomethylene)-indanone))-5,5,11,11-tetrakis(4-hexylphenyl)-dithieno[2,3-*d*:2′,3′-*d*′]-*s*-indaceno[1,2-*b*:5,6-*b*′]dithiophene (ITIC) and its methyl derivative (ITIC-M) have been intensively studied in combination with low-bandgap polymers due to their high performance (beyond 12%).[10] When ITIC was blended with P3HT, however, the system resulted in very low electron mobility[30] and PCEs below 2%.[31] Besides the device performance, a theoretical study on colour tuning recently revealed that NFAs are the best approach to tune the aesthetic appearance (*i.e.* colour) of P3HT based solar cells.[9]

With very few exceptions, in most of the reported studies exploring NFA based OPVs, the devices are manufactured by spin-coating, which is not an up-scalable technique. Very recently, Strohm *et al.* demonstrated P3HT:O-IDTBR laser-patterned modules manufactured by doctor blading and slot-die coating.[32] In their work, solvent screening was carried out in order to identify promising 'greener' solvent systems. This work, as well as other papers,[33,34] indicated that the whole processing scheme needs to be revisited when moving from spin coating to blade coating. With the aim of advancing towards the mass production of OPVs, it is thus clear that further studies on the compatibility of P3HT with different NFAs manufactured using more scalable techniques will be desirable, including on the role of different solvents and the effect of the processing parameters such as processing temperatures and annealing steps.

In this contribution, we have provided such investigations making use of high throughput processing screening of five doctor-bladed P3HT:NFA systems. More precisely, we have fabricated over 1000 solar cells based on ITIC, ITIC-M, O-IDTBR, EH-IDTBR, O-IDFBR and two fullerene references ($PC_{60}BM$ and ICBA). This set of acceptor materials allows us to study the effect of the acceptor type (fullerene *vs.* NFA), the NFA side chains and the end-capping group, as well as the aggregation tendency of the materials. Once we identify the best potential candidate to blend with P3HT, we can study relevant parameters for the scalability such as thickness dependence, solvent system, annealing temperature and casting temperature. Finally, we carry out a long-term stability test as a function of the photoactive layer (PAL) thickness and encapsulation. The latter study is very relevant from the industrial perspective since we find that the most efficient devices are not necessarily the most long-term stable devices.

## Experimental

### Solar cell fabrication

All devices were manufactured with an inverted architecture (glass/ITO/ZnO/PAL/$MoO_3$/Ag). ITO substrates (purchased from Ossila, 100 nm thick and 20 Ω per square sheet resistance), were cleaned by sequential ultrasonication in acetone, a Hellmanex 10% solution in water, isopropanol and finally a 10% NaOH water solution. As the electron transport layer (ETL) material, ZnO nanoparticle dispersions (N-10, Avantama) were blade coated onto pre-cleaned ITO substrates in air using an automatic coater (ZAA 2300, Zehntner) and lamination equipment (ZUA 2000, Zehntner). The ZnO casting parameters were 50 μm blade gap, 50 μL cast volume, 4 mm $s^{-1}$ blade speed and a casting temperature of 40 °C yielding a thickness of 40 nm. A 100 °C post-deposition thermal annealing was carried out for 10 min in air. The ZnO coated substrates were then transferred into a nitrogen-filled glovebox for the deposition of the photoactive layers. The chemical structures of all acceptors, namely ITIC, ITIC-M, O-IDTBR, EH-IDTBR, O-IDFBR, $PC_{60}BM$ and ICBA, are shown in Fig. 1. All NFAs were purchased from 1-Material except for O-IDTBR (purchased from Sigma-Aldrich) and fullerenes were purchased from Solenne. Both semiconductors, P3HT and acceptors, were dissolved in either chlorobenzene (CB) or CB:dichlorobenzene (DCB), with a weight fraction of P3HT:acceptor of 1 : 1 and with a total solid concentration of 15 mg $mL^{-1}$. The typical processing conditions for P3HT:acceptor devices were a blade gap of 100 μm, a casting volume of 70 μL and a casting temperature ranging from 40 °C to 105 °C.

In order to rapidly screen the processing conditions, we have employed samples with gradients in two parameters of interest, thickness and thermal annealing temperature.[35] For the first one, a home-made speed controller was coupled to the blade coater. Photoactive layers were deposited by decelerating the blade from 90 mm $s^{-1}$ to 5 mm $s^{-1}$ during solution spreading across the 7 cm length of the substrate. This variable speed leads to a thickness gradient of the sample in the photoactive layer, which typically varies from 200 to 50 nm (the exact values depend on the processing parameters of the gradient). Fig. S1† shows photographs of representative devices exhibiting

 

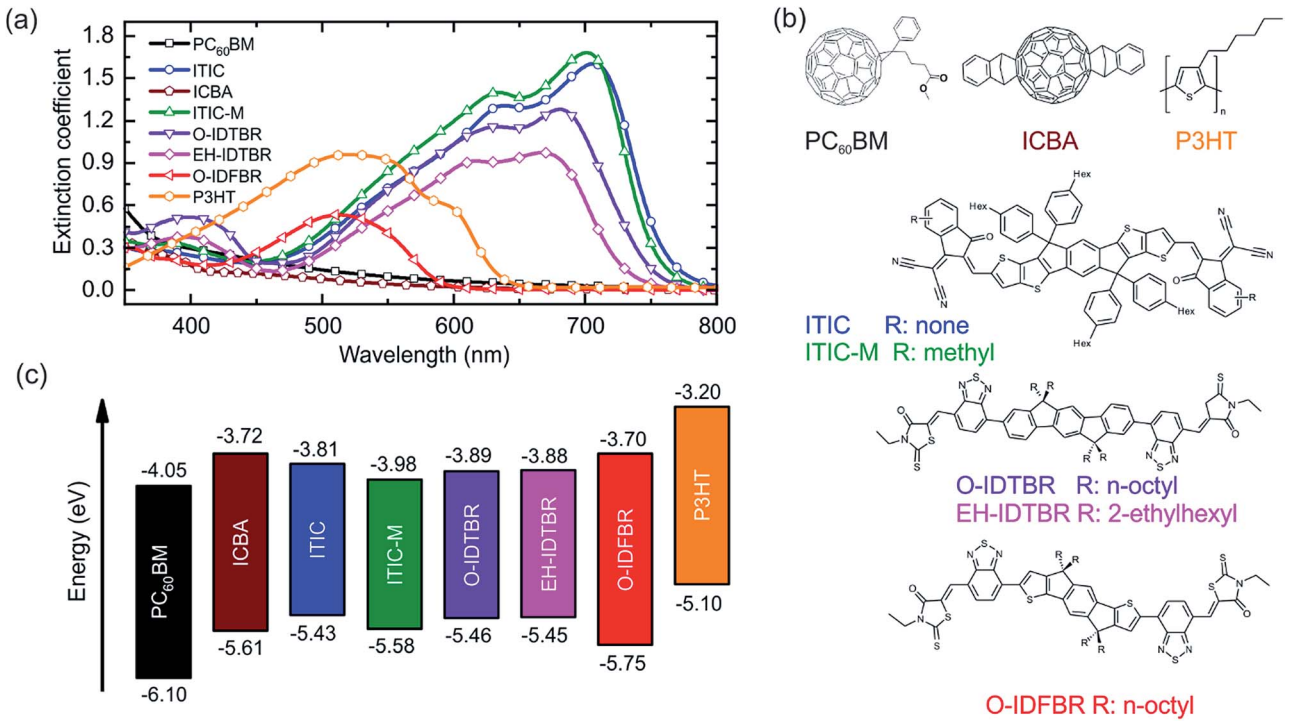


Fig. 1 Material properties for the studied systems, namely P3HT, $PC_{60}BM$, ICBA, ITIC, ITIC-M, O-IDTBR, EH-IDTBR, and O-IDFBR. (a) The extinction coefficient obtained by VASE, (b) chemical structures and (c) energetic levels (obtained from the literature with the corresponding references given in the main manuscript).

thickness gradients for the seven evaluated binaries. Furthermore, these thickness gradients are analyzed by both optical characterization (Fig. S2 and S3†) and/or mechanical profilometry. This approach enables rapid evaluation of the thickness dependence of each combination.[35,36] A second type of graded-sample consists of applying a post-deposition thermal gradient annealing on samples exhibiting a homogeneous thickness. This is carried out by using a Kofler bench, which is a hot plate with a position-dependent temperature. The 12 devices on each side of the substrate were all exposed to slightly different temperatures through the annealing gradient. The Kofler bench exhibits a thermal gradient of 6.7 °C $cm^{-1}$ and a temperature range extending from 30 °C to 200 °C. Finally, 10 nm of $MoO_3$ (hole transporting layer, HTL) and 100 nm of Ag were thermally evaporated at a rate of 0.1 and 1 Å $s^{-1}$, respectively.

Each sample contains 24 devices, 12 of them with different thicknesses or thermal annealing (two per side), with a pixel active area of 8 $mm^2$ (see Fig. S1†). Before electrical characterization, all devices were annealed on a hot plate inside a glovebox at 120 °C for 20 min. For the long-term aging study, OPV devices were encapsulated with a glass slide and sealed with a UV-curable epoxy resin (Ossila) in the glovebox.

### Solar cell characterization

*J–V* characteristics were automatically obtained by using a Keithley source meter and an Arduino based multiplexer/switcher which allows measuring 24 devices in less than 6 minutes. As a lighting source, a SAN-EI Electric XES-100S1 AAA solar simulator was used to ensure a homogeneous illumination in a 10 cm × 10 cm area. The solar simulator was previously calibrated with a certified silicon solar cell (Oriel). External quantum efficiency (EQE) was measured with a home-made system that uses a Supercontinuum light source (4W, Fianium) coupled to a monochromator and normalized by the light power as measured by a silicon diode. We have measured EQEs from 400 nm to 900 nm wavelength by focusing the laser on a spot of 50 μm in diameter.

### Thin film characterization

Reflectance spectra were measured with a Fourier-transform spectrophotometer (Vertex 70, Bruker) with a 4× magnification objective and the wavelength scanned from 400 nm to 900 nm. The optical density was measured by recording the transmitted light (HL-2000-LL, Ocean Optics) within an integrating sphere by means of a spectrometer (FLAME-S-VIS-NIR-ES, Ocean Optics). Contact angle measurements (DSA 100, KRÜSS) were carried out using 5 μL distilled water drops that were monitored using image analysis software in order to obtain the contact angle value. The complex refractive indices were calculated from variable angle spectroscopic ellipsometry (VASE) data using a Semilab GES5E rotating polarizer ellipsometer. Modelling of the ellipsometry data was performed using the Winelli II software package from SOPRALAB. The film thickness was measured using a mechanical profilometer (Dektak 150, Bruker). The surface morphology of the blend films was examined using an atomic force microscope (AFM) in

tapping mode configuration (Keysight 5100, Agilent). X-ray diffraction (XRD) spectra of the blend films were collected using an X-ray diffractometer (A25 D8 DISCOVER, Bruker) with grazing incidence geometry. Cu K$\alpha$ radiation ($\alpha$ = 1.54 Å) was used with a scanning angle ($2\theta$) ranging from 3° to 60°. Raman scattering spectra were acquired using a WITec alpha 300 RA$^+$ confocal Raman setup. The samples were excited through a 10× objective using two solid state lasers centred at 488 nm and 785 nm. The Raman spectra were analysed using WITec Project FOUR software and fitted with Fityk software.[37]

## Results and discussion

### Physical properties of semiconductors

The type of acceptor (fullerene or small molecule-NFA) has a strong influence on the absorption spectrum of the P3HT binary. Thus, the extinction coefficients for the different materials, as obtained by variable angle spectroscopic ellipsometry (VASE), were measured and are shown in Fig. 1(a). This set of NFAs can harvest light efficiently from 450 nm to 750 nm depending on the molecule, while $PC_{60}BM$ is known to barely contribute to the overall absorption of the blend. The high absorption of NFAs can be exploited for tuning the aesthetics of P3HT based solar cells.

Binaries of P3HT:fullerene typically have a brownish appearance; however the addition of NFAs to the blend allows tuning the chromaticity from purple (ITIC, ITIC-M, and IDTBR) to reddish (O-IDFBR) as Fig. S2† shows. Moreover, the specific NFA side chains (Fig. 1(b)) also have an influence on the absorption. For instance, octyl side chain (O-) decorated IDTBR shows red-shifted and stronger absorption peaks compared to the ethyl-hexyl (EH-) counterpart. This effect is mainly attributed to the different degree of crystallinity of the two variants.[19,38] On the other hand, methyl-end-capping groups on ITIC show almost no difference in light absorption compared to ITIC (Fig. 1(a)). Interestingly, except for O-IDFBR, this set of NFAs has complementary absorption with respect to P3HT, which enables extending the light absorption from 400 nm to 800 nm. We, thus, may expect an increased short-circuit current ($J_{sc}$) of the corresponding solar cells compared to those based on the conventional $PC_{60}BM$ or ICBA fullerene.

The energy levels of the considered donor and acceptor materials are shown in Fig. 1(c), as obtained from the literature.

In general, the optical gaps inferred from absorption are well correlated to the reported energy levels. When comparing materials, and in contrast to the effects described for absorption, end-capping groups (ITIC *vs.* ITIC-M[39]) have a higher influence on the energy levels than side chain modifications (O-IDTBR *vs.* EH-IDTBR).[19] The addition of the methyl end-capping groups shifts the LUMO and HOMO levels up to 0.17 eV and 0.15 eV, respectively. The modification of the side chains in IDTBR does not appreciably vary the energy levels of the molecule. Nevertheless, the acceptor type is not the most defining factor in this case. While the LUMO of $PC_{60}BM$ and ICBA lies at −4.05 eV and −3.72 eV, respectively, energy levels of NFAs can also be tailored and designed from −3.70 eV (O-IDFBR[26]) to −3.98 eV (ITIC-M). Increasing LUMO levels of the acceptor and maintaining low HOMO levels implies an enhancement in the open circuit voltage ($V_{oc}$), provided that the materials show similar levels of recombination. For instance, and as reported, the increase of O-IDFBR and ICBA LUMO levels to −3.70 eV and −3.72 eV (compared to the −4.05 eV of $PC_{60}BM$) leads to enhanced $V_{oc}$ values of 0.9 V and 0.83 V, respectively, of the corresponding solar cell (*cf.* 0.6 V for $PC_{60}BM$[26]).

### Performance of P3HT based solar cells

The JV characteristics of the best performing blade-coated P3HT based systems are shown in Fig. 2(a). According to these results, we might split the considered acceptors into two main groups: P3HT working systems and P3HT non-working systems. On the one hand, non-working P3HT:NFA systems when blended with P3HT, such as ITIC and its derivative, ITIC-M, show a very modest performance despite their promising optical properties

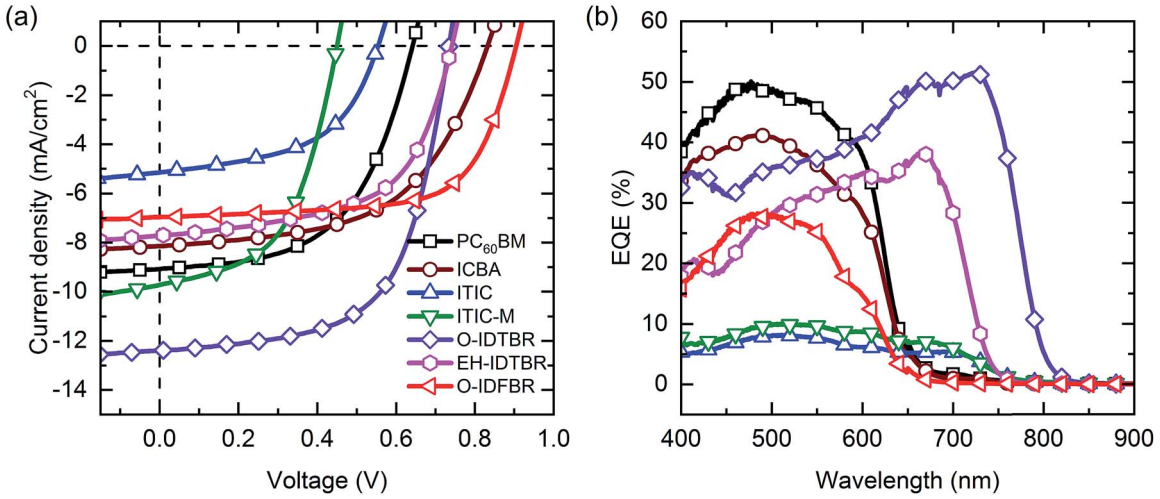


Fig. 2 (a) *J*–*V* characteristics and (b) external quantum efficiency (EQE) of P3HT based systems. P3HT is mixed with seven acceptor materials, namely $PC_{60}BM$, ICBA, ITIC, ITIC-M, O-IDTBR, EH-IDTBR and O-IDFBR.

Table 1 Photovoltaic parameters of the doctor bladed champion solar cells based on P3HT mixed with $PC_{60}BM$, ICBA, ITIC, ITIC-M, O-IDTBR, EH-IDTBR and O-IDFBR. For device statistics and reproducibility of the high throughput method, see Fig. S5

| Acceptor | $V_{oc}$ (V) | $J_{sc}$ (mA cm$^{-2}$) | FF (%) | PCE (%) |
|---|---|---|---|---|
| $PC_{60}BM$ | 0.64 | −9.1 | 54.6 | 3.2 |
| ICBA | 0.83 | −8.2 | 54.8 | 3.7 |
| ITIC | 0.55 | −5.2 | 52.2 | 1.5 |
| ITIC-M | 0.45 | −9.8 | 52.5 | 2.3 |
| O-IDTBR | 0.74 | −12.4 | 61.6 | 5.6 |
| EH-IDTBR | 0.74 | −7.7 | 57.7 | 3.3 |
| O-IDFBR | 0.90 | −6.9 | 67.5 | 4.2 |

and the *a priori* good energy level alignment.[31] Fig. 2(b) shows that P3HT:ITIC based systems have an external quantum efficiency (EQE) below 10%, in agreement with the literature and their 1 sun *JV* curves.[31] Fig. S4† shows that none of the ITIC based solar cells follow the expected linear behaviour between the measured and theoretical $V_{oc}$.[40] This fact can be attributed to very strong recombination processes and therefore, higher voltage losses. This interpretation agrees with literature studies that report very low PCE values for the P3HT:ITIC system due to the high degree of crystallinity and consequently large phase separation.[31] On the other hand, the group of acceptors that we found to be blade coating compatible with P3HT include $PC_{60}BM$, ICBA, O-IDTBR, EH-IDTBR and O-IDFBR. The PCE of these P3HT systems extends from 3.2% for $PC_{60}BM$ to 5.6% for O-IDTBR (for the reproducibility of this optimization methodology see Fig. S5†). Among the working systems, the $PC_{60}BM$ blend shows the poorest performance mainly due to the lower open circuit voltage compared to those of NFA based mixtures. The $PC_{60}BM$ based system achieves 0.64 V whereas the rest of the working NFA systems achieve 0.7 V, reaching up to 0.9 V for O-IDFBR. This drop in voltage is explained by the lower LUMO level of $PC_{60}BM$ with respect to those of the NFAs (Fig. 2(a) and Table 1). Interestingly, the other fullerene reference, ICBA, exhibits a PCE of 3.7% due to the large $V_{oc}$. The theoretical and measured $V_{oc}$ values for the P3HT working systems follow a linear trend (Fig. S4†) suggesting small recombination losses. For the $V_{oc}$ values of the P3HT working systems, there is good agreement between the measured and the reported data. Another relevant factor is the large influence of the side chains of the NFAs on the final performance. The cells prepared with octyl side chains (O-IDTBR) exhibit much larger short-circuit current density (12.4 mA cm$^{-2}$) compared to those prepared with ethylhexyl side chains (EH-IDTBR) (7.7 mA cm$^{-2}$). EQE spectra are in agreement with $J_{sc}$ values for the different NFAs. The IDTBR molecule with linear side chains (O-IDTBR) has a red-shifted spectrum and harvests light more efficiently for all wavelengths compared to that with the branched one (Fig. 2(b)). Clearly, the side chains affect not only the molecular solubility for a given solvent system but also the final morphology of the photoactive layer. Moreover, this points to a strong morphology dependence of the device performance, as is often seen for P3HT based devices. This fact might help to explain why the ITIC family exhibits such poor performance.

### Selection of studied parameters and sensitivity analysis

The record P3HT:acceptor based solar cells used here as a reference are typically processed from CB, manufactured by spin-coating and subjected to post-thermal annealing. We look at the parameters that typically have a high impact on the device performance when moving from spin-coating to blade-coating. These parameters are the solvent system, the annealing-temperature and the typical parameters for blade coating such as blade-speed (thickness) and casting temperature.

For a given material system, the precise control of the parameters that affect the crystallinity of the films is also crucial for device optimization. The most used solvent system in the spin-coating technique is CB, albeit in some cases the addition of precise amounts of a solvent additive, such as 1,8-diiodooctane, can improve the degree of phase separation and thus the morphology of the blend.[41] In this work we compare CB and a binary mixture of universal solvents (CB:DCB) to process the P3HT:acceptor system. Compared to that of additives, the exact solvent weight fraction may be less critical, and thus this choice is more general. We also looked at the blade coating temperature, as a means of modifying the drying kinetics without specifically changing the solubility of materials. Typically, the top-performing blade-coated solar cells are cast around 80–90 °C. In this study, the casting temperature was also varied from 40 °C to 105 °C. To investigate the thickness–performance dependence, the blade speed was varied from 5 to 99 mm s$^{-1}$. Finally, the effect of the post annealing temperature was studied by varying the annealing temperature gradually from no-annealing to 150 °C. It is within this range of temperatures that P3HT-based solar cells usually show their optimum annealing temperature.

Since there are many variables involved in the optimization process of blade coated P3HT:acceptor based devices, sensitivity analysis was carried out in order to identify the most critical parameter/s. For this, the F-statistics obtained by statistical one-way analysis of variance (ANOVA) was used to individually assess the effect of each processing parameter of the dataset.[42] The statistical parameter ANOVA-F is defined as the variance ratio between the independent variable (solvent system, casting temperature, annealing temperature and blade speed) and the variation within the dependent variable (power conversion efficiency). A large ANOVA-F value suggests highly sensitive parameters whereas a small one reveals a parameter with low relevance in the overall optimization process.

The ANOVA-F values for the studied parameters are summarized in Table S1,† and they reveal that the most sensitive performance parameter of P3HT:acceptor based devices is the acceptor material ($F = 129$), as shown in the previous section. While O-IDTBR devices achieve efficiencies over 5.5%, ITIC based devices only yield 1.5% (Fig S6†). Then, the second most sensitive parameter ($F = 84$) is the solvent system. In the case of P3HT:O-IDTBR based devices, the performance varies up to 1.7% for a binary solvent system. Then, the effect of the annealing temperature is crucial for P3HT based devices ($F = 64$) with variations of more than 0.6% of efficiency to achieve a proper balance between crystalline and amorphous domains

of both components. Finally, the least sensitive among the studied parameters are the casting temperature ($F = 40$) and, to a lesser extent, the blade speed, equivalent to the active layer thickness. The variation in performance upon thickness variation is less than 0.5% whereas the casting temperature varies less than 0.3% in the scanned temperature range. Our study indicates that, as a rule of thumb, the most critical OPV parameters are first the choice of materials, then the precise microstructure, and finally the geometrical device factors. In the following sections, we analyse individually the contribution of each of the parameters starting from the solvent system and the acceptor material.

### Meta-analysis of P3HT based solar cells

We have carried out a data science inspired study of solar cells having P3HT as the donor. With the aid of a home-made database, more than a thousand P3HT based devices were considered and are summarized in Fig. 3. For clarity, we fixed threshold values, namely solar cells with a $V_{oc}$ greater than 0.3 V, FF greater than 30% and PCE greater than 0.5%. The number in brackets in Fig. 3 represents those devices that overcame the threshold. For instance, the same number of ITIC and ITIC-M based devices were manufactured; however, only 1 ITIC based device processed from CB achieved a PCE larger than 0.5%. Moreover, this box and whisker plot is a summary of the optimization process and thus the plot includes variations in the photoactive layer thickness, annealing temperature, casting temperatures and solvents. This is the reason for the large dispersion of the data (such as $J_{sc}$ and FF, which are highly solvent-processing sensitive).

As a general trend, for any given material, we have found that the solvent system is the second most sensitive parameter in P3HT-based devices (see ANOVA sensitivity analysis). This suggests that solar cells processed by doctor blading are quite sensitive to the drying kinetics. Introducing a solvent with a higher boiling point (131 °C and 180 °C for CB and DCB, respectively) delays film formation affecting domain formation.

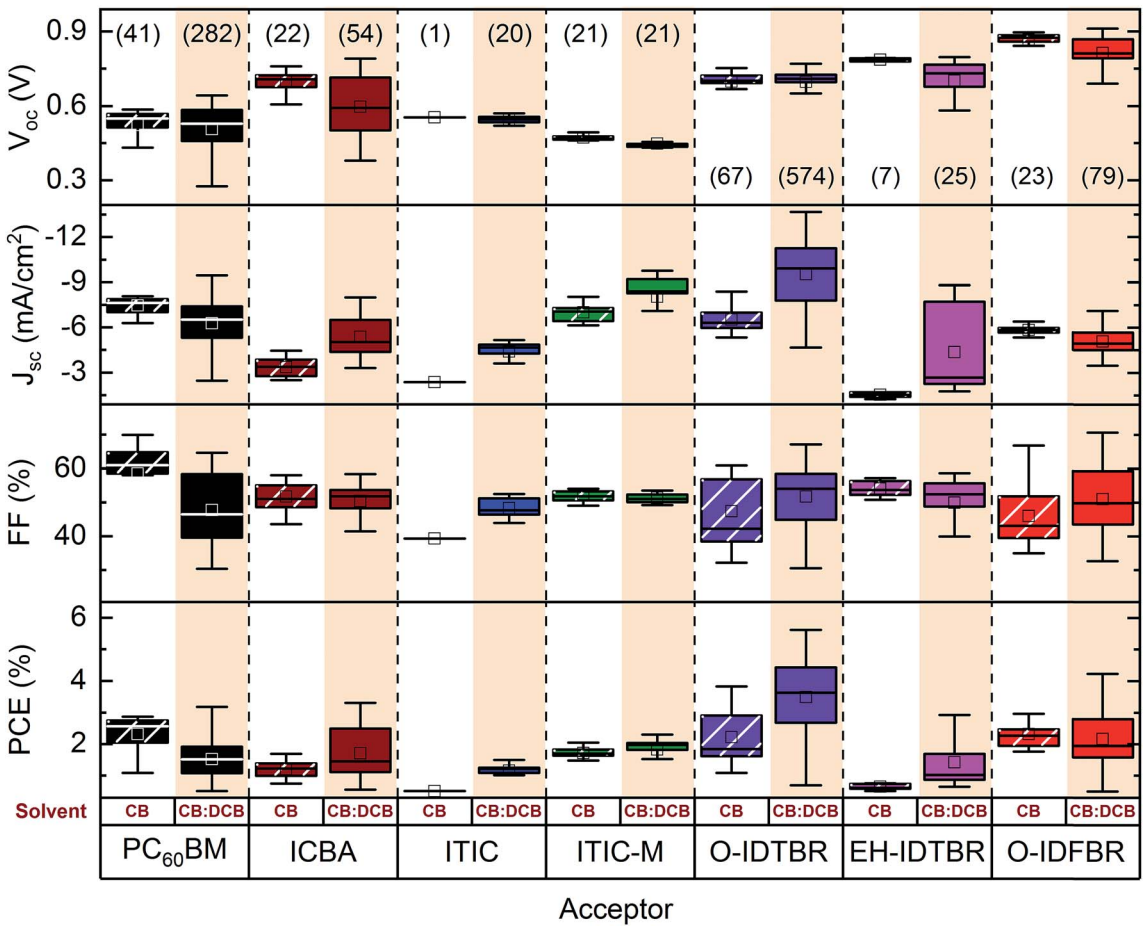


Fig. 3 Box and whisker plot of photovoltaic parameters from 1560 devices of P3HT blended with seven different acceptor materials ($PC_{60}BM$, ICBA, ITIC, ITIC-M, O-IDTBR, EH-IDTBR, and O-IDFBR) as a function of the solvent, namely chlorobenzene (CB) and a mixture of chlorobenzene:dichlorobenzene (CB:DCB). The photovoltaic parameters are open circuit voltage ($V_{oc}$), short-circuit current ($J_{sc}$), fill factor (FF) and power conversion efficiency (PCE). Data include thickness variations, annealing temperature variations, several casting temperatures and various volume ratios. Statistical values are represented by mean (inner empty square), median or 2nd quartile (inner horizontal line), 1st and 3rd (height of the box) and maximum and minimum value (whisker height). The number of devices characterized for each material system is shown in brackets (only those which overcome the 0.5% PCE and 30% FF threshold) on the top row.

 

This first conclusion prompts a detailed investigation of the deposition temperature and post-deposition annealing temperature (see following sections).

Photovoltaic parameters like $J_{sc}$ or FF are very sensitive to variations in the processing parameters. The first observation is that, consistently, the highest values of $J_{sc}$ and FF are always obtained for cells processed from CB:DCB, regardless the choice of NFA, side chains, or end-capping group. This effect is particularly pronounced in IDTBR cells with both types of side chains considered: the $J_{sc}$ doubles when processed from CB:DCB.

Unlike the $J_{sc}$, FF is not as affected by the solvent choice. Unsurprisingly, the systems with higher dispersion of FF are $PC_{60}BM$ and O-IDTBR, which are those with more than 280 devices each. The O-IDFBR system exhibits the highest FF, 67%, which is quite close to the values reported in the literature for spin coated cells.[26] However, since the overall absorption is low, the final efficiency is low as well. This problem has been tackled by introducing O-IDTBR in the binary system to enhance $J_{sc}$.[26]

The solvent system has a low impact on $V_{oc}$. CB and CB:DCB processed devices show similar $V_{oc}$ values with a dispersion below 0.1 V considering median values. Interestingly, processing with CB:DCB leads to a higher $V_{oc}$ in $PC_{60}BM$ and a slightly lower $V_{oc}$ in ICBA, EH-IDTBR and O-IDFBR. These small variations in $V_{oc}$ values typically arise from small changes in the degree of crystallinity of the photoactive layer.[43]

Finally, the power conversion efficiency (PCE) reveals that the most promising NFA blended with P3HT is O-IDTBR. Despite the many processing parameters varied in the study, the median PCE of O-IDTBR cells is above 4% whereas the median of the other systems mixed with P3HT does not exceed 3%. The PCE mainly reflects the dependence of $J_{sc}$ on the solvent system. Consistently, higher PCE values are found for cells based on CB:DCB mixtures. According to this study, we can affirm that systematically and under different conditions, the most efficient option among the studied set of NFAs for blending with P3HT is O-IDTBR. In addition, this finding is also supported by Strohm *et al.* who found that combinations of CB with a precise small addition of *p*-bromoanisole (5.6%) outperformed the inks processed from pristine CB (2.6%).[32] Interestingly, in our study, blade-coated P3HT:O-IDTBR devices with over 4% PCE were processed from pristine CB.

## Solvent study: contact angle and thickness dependence for the P3HT:O-IDTBR system

In order to understand the origin of the better performance of devices processed from CB:DCB mixtures, we studied the P3HT:O-IDTBR system in depth.

It is worth highlighting that the study as a function of the solvent and thickness was carried out following the high-throughput approach and using only two substrates. This high-throughput approach enables saving both time and resources when evaluating an OPV system.[35] In this approach, the blade is gradually decelerated during coating resulting in a sample with a thickness gradient.[35] In order to ensure the reproducibility of this approach, we prepared three P3HT:O-IDTBR solar cells under the same processing conditions which yielded comparable PCE results and thickness trends for the thickness sweep explored (from 50 nm to 180 nm; see Fig. S5†). Fig. 4a and b show the $J_{sc}$ and PCE of P3HT:O-IDTBR devices processed from CB and CB:DCB. The latter exhibit, consistently, higher $J_{sc}$ compared to CB based devices, with a milder thickness dependence. More precisely, there is a $J_{sc}$ enhancement of more than 4 mA $cm^{-2}$ for devices processed from the solvent mixture with thicker films (200–300 nm). Unlike $J_{sc}$, FF and $V_{oc}$ do now show large differences based on the solvent system (see Fig. S7†). The enhancement of $J_{sc}$ observed for a mixture of solvents is usually explained by a higher degree of crystallinity, better domain size and/or purity or by improved vertical segregation.[44,45]

In order to evaluate the effect of the solvent choice, the water contact angles of the neat donor and acceptor materials, P3HT and O-IDTBR, were measured together with those of blends deposited from CB and CB:DCB. The contact angle values for neat P3HT and O-IDTBR processed from CB (Fig. 4(c) and (d)) are 98.1° ± 1.2° and 108° ± 2.0°, respectively, and thus they are easily distinguishable. Additionally, to rule out the effect of the processing solvent on the wetting properties of the neat material, we measured the contact angle of the P3HT film processed from CB:DCB which showed a similar value (107.5° ± 0.9°) when processed from CB. On the other hand, it was not possible to cast O-IDTBR on glass when it is processed from the mixture of solvents. Fig. 4(e) depicts the contact angle of the photoactive layer coated from CB, which corresponds to the average contact

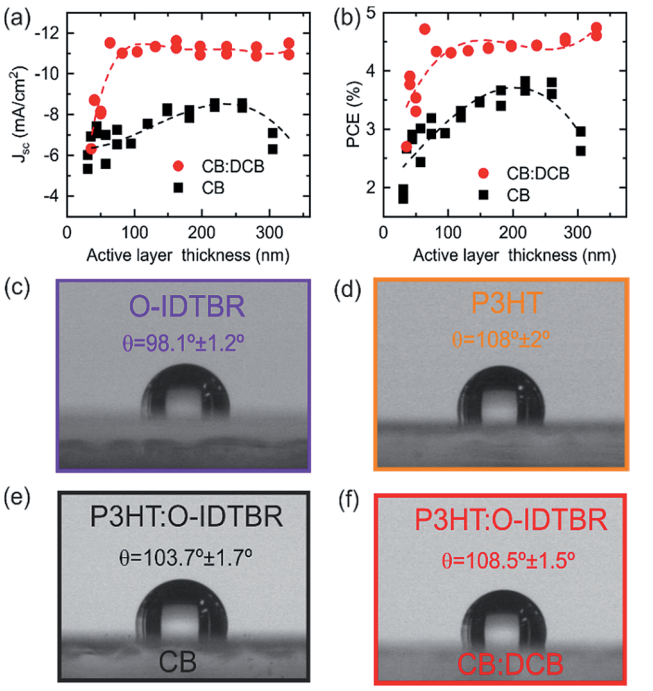


Fig. 4 Solvent and thickness dependence study on P3HT:O-IDTBR cells. (a) Short-circuit current density and (b) PCE as a function of the photoactive layer thickness and the solvent system (dashed lines are plotted as a guide to the eye). Contact angle measurements on glass for neat materials processed from CB:DCB: (c) O-IDTBR and (d) P3HT, and blends P3HT:O-IDTBR (e) from CB and (f) from CB:DCB.

angle value of both P3HT and O-IDTBR. However, the photoactive layer manufactured from CB:DCB (Fig. 4(f)) leads to a contact angle equal to that of the neat P3HT. The contact angle measurements strongly suggest preferential segregation of P3HT domains towards the surface of the photoactive layer. This finding supports the construction of the inverted structure of the cell where the donor electron (P3HT) material should be placed close to the hole transporting layer.

The degree of crystallinity was also evaluated using spectroscopy. First, optical absorption measurements show little change in the absorption of the NFA when going from CB:DCB to CB (Fig. S8a†). Second, to understand the role of P3HT, Raman scattering measurements were also carried out (Fig. S8b†). The P3HT Raman cross-section is much higher than that of O-IDTBR; thus the observed Raman peaks can be uniquely attributed to P3HT. Following the literature, we have analysed the main P3HT Raman bands as a superposition of two components, namely regio regular (RR) and regio random (RRa) (Fig. S9†).[46] Table S2† shows a summary of the Raman peak analysis. The higher RR/RRa height peak ratio for films processed from CB compared to those made from CB:DCB suggests that the former lead to higher P3HT crystallinity.

To confirm the Raman results, we used X-ray diffraction measurements (XRD). XRD diffraction spectra of P3HT:O-IDTBR films processed from CB and CB:DCB are shown in (Fig. S10†). The XRD spectra show a P3HT (100) intense peak at 5.3° which is in agreement with previous reports.[47] The intensity of the P3HT peaks of films processed from CB is higher than that of CB:DCB processed films of a similar thickness, with the FWHM of the latter being slight smaller (0.027 $Å^{-1}$ and 0.029 $Å^{-1}$ for CB and CB:DCB, respectively). Therefore, the XRD findings are in agreement with the Raman scattering results revealing an excessive degree of crystallinity of P3HT blends when processed from CB compared to CB:DCB.

Finally, atomic force microscopy (AFM) was used to investigate the effect of the processing solvent on the surface of P3HT:O-IDTBR blend films. The topography and height images are shown in Fig. S11.† CB:DCB processed films have a more uniform surface with a lower root-mean-square (RMS) of 9 nm than CB (15 nm). Additionally, the CB processed films display large aggregation in the range of micron sizes which is typically related to the crystallinity of the material. By contrast, the morphology of the CB:DCB processed films evolves to a more favorable donor–acceptor phase separation. The better intermixing morphology together with lower RMS explains the higher $J_{sc}$ and charge transfer for CB:DCB compared to CB processed films.

In summary, Raman, XRD and AFM measurements suggest that the mixture of solvents prevents large scale phase separation, as recently suggested for a different solvent mixture.[20] As we will see in the next section, the optimum degree of phase separation and the controllable crystallinity are key for high performing devices.

### P3HT:O-IDTBR thermal annealing study

The solvent study presented in the previous section clearly shows that the attained blend morphology is a very important parameter determining the final device photocurrent for devices based on P3HT and NFAs.

In particular, the CB:DCB solvent system induces a more appropriate degree of P3HT crystallinity yielding higher efficiencies compared to CB. Alternative processing schemes aimed at tuning the morphology of the photoactive layer include optimizing the casting temperature and the post-deposition thermal annealing temperature. In this section, we investigate the effect of thermal annealing temperature on the performance of P3HT:O-IDTBR solar cells processed from CB:DCB. A high throughput approach was again employed; in this case a sample of constant thickness was exposed to an annealing temperature gradient using a Kofler bench (see the Experimental section).

The performance of the as-cast samples is shown in Fig. 5(b) and S12.† Non-annealed samples show a low FF (40%) and a modest $J_{sc}$ (10 mA $cm^{-2}$). Interestingly, both the PCE (Fig. 5(b)) and FF (Fig. 5(a)) were achieved under optimum annealing conditions around 120 °C, while the $J_{sc}$ is maximized at slightly higher temperatures (Fig. S12†). Note that the minimum annealing temperature was 105 °C, corresponding to the deposition temperature. This fact suggests that the FF is the dominant parameter affected by the annealing temperature. Increasing the annealing temperature above 120 °C leads to a progressive decrease of both the FF and PCE, presumably due to the development of larger crystalline domains (Fig. 5(c)). Moreover, the FF (PCE) decreases from 52% (4.3%) to 42% (3.7%) upon annealing at 120 °C and 150 °C, respectively. Annealing promotes NFA crystallization, as clearly reflected by the bathochromic shift in the absorption spectra produced by annealing (Fig. 5(c)). Note that the absorption change observed upon annealing occurs in the spectral region corresponding to NFA absorption, while the overlapping absorption of the two components around 500 to 650 nm makes it difficult to assign changes in P3HT crystallinity with confidence. To evaluate whether P3HT also shows increases in crystallinity upon annealing, we have performed Raman scattering studies on the devices.[46,48] The Raman analysis reveals that the RR/RRa peak height ratio (degree of crystallinity) increases with temperature (Table S2†). Moreover, the optimum RR/RRa peak height ratio for films of P3HT:O-IDTBR processed from CB:DCB is 4.5 (Fig. S9†). An RR/RRa ratio larger than 4.5 leads to a reduction in the performance of the solar cell. Interestingly, the as-cast P3HT:O-IDTBR films from CB show a similar degree of crystallinity (RR/RRa height ratio), namely 5.6, and 3.5% PCE (Fig. 4(b)), which are comparable to those of the 150 °C-annealed CB:DCB processed devices leading to a RR/RRa ratio of 6 and 3.8% PCE. This is clear evidence that the control of the morphology results in a trade-off between the solvent system and annealing temperature. In summary, the degree of P3HT crystallinity can be optimized with the choice of solvent, while that of O-IDTBR can be optimized through the post-deposition annealing temperature. For comparison, a similar annealing temperature dependent study was carried out for the P3HT:O-IDFBR system (details in Fig. S13†). Interestingly, the optimum annealing temperature is, in this case, around 150 °C, which is close to the typical temperature needed to optimize P3HT:$PC_{60}BM$ blends, which has been attributed to the

 

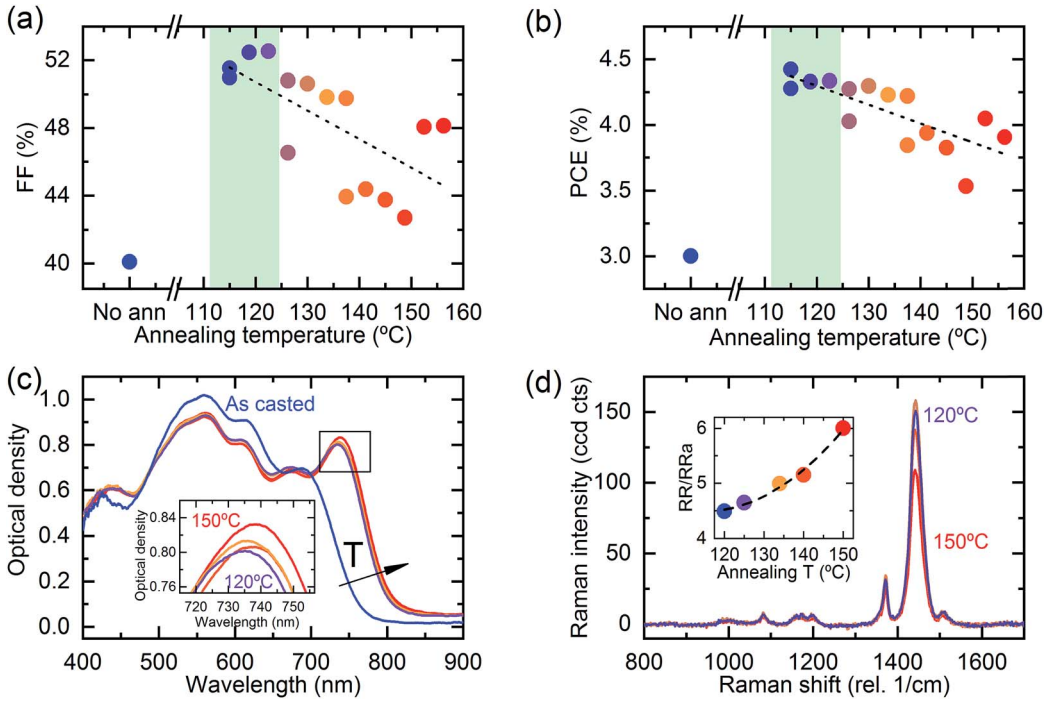


Fig. 5 Annealing temperature effect on P3HT:O-IDTBR solar cells processed from CB:DCB. (a) Fill factor and (b) performance as a function of the annealing temperature. (c) Optical density spectra. Inset: absorbance in the zoomed-in wavelength range of interest from 710 to 770 nm. (d) Raman shift of photoactive layers annealed at temperatures from 120 °C to 150 °C. Inset: Raman peak height ratio of regio regular (RR) and regio random (RRa) P3HT components. In all graphs, a temperature–colour dependent scale is used. Colours vary gradually from no annealing (blue) to 150 °C annealing (red). Dashed lines are plotted as a guide to the eye.

temperature required to crystallize P3HT.[49] Considering that O-IDFBR molecules partially prevent P3HT crystallization, it is reasonable that the temperature required to enhance its crystallinity is higher.[26] Correspondingly, the controlling photovoltaic factor appears to be the combination of $J_{sc}$ and FF, as one may expect from an improved degree of crystallinity and thus charge transport upon annealing.

### Study of the casting temperature for the P3HT:O-IDTBR

After analysing the solvent system and the post-annealing temperature, in this section we will investigate the role of the deposition temperature.

Fig. 6 shows the photovoltaic parameters of P3HT:O-IDTBR solar cells with a thickness gradient cast at 3 different temperatures (40 °C, 80 °C and 105 °C). The OPV devices in this study were also thermally annealed at 120 °C after casting (at the optimum annealing temperature previously found). Devices cast at 80 °C and 105 °C exhibit a $V_{oc}$ around 0.72 V, whereas devices cast at 40 °C show a slightly lower $V_{oc}$ (0.70 V). Moreover, Fig. S14† shows red-shifted absorption peaks for devices cast at 40 °C compared to those of samples deposited at 80 °C and 105 °C. This indicates that slower drying dynamics leads to a higher degree of NFA crystallinity.

The $J_{sc}$ of the devices cast at different temperatures exhibits a similar trend to photoactive layer thickness with the first interference peak at a blade speed of 40 mm $s^{-1}$, which corresponds, in this case, to a thickness of 120 nm. $J_{sc}$ for the three casting temperatures reaches a value of 12 mA $cm^{-2}$. Interestingly, $J_{sc}$ shows the same increasing trend with no effect of the casting temperature despite the different drying kinetics. This strong effect indicates that the post-deposition annealing partially erases the processing history of the film, provided that the deposition temperature is below the post-deposition annealing temperature. This type of thermal memory effect has been observed before in conjugated polymers subjected to cyclic thermal annealing.[50] Unlike the $J_{sc}$, the highest FFs are found for the devices cast at 40 °C. This effect might be explained by the slow drying, and thus longer duration for domain formation, in agreement with the EQE and absorption spectra (Fig. S14†). Finally, the PCE reveals that this combination of semiconductors is not especially sensitive to film thickness. Promisingly, PCE values above 5% are obtained for deposition temperatures ranging from 40 °C to 105 °C and for blade speeds ranging between 35 mm $s^{-1}$ and 80 mm $s^{-1}$. This finding makes this OPV system an interesting candidate for upscaling since the processing windows resulting in high efficiency are large.

### Ageing study of P3HT:O-IDTBR solar cells

Long-term stability is also a key factor to ensure that OPVs reach the market. In order to increase the energy returns on investment, high efficiency solar cells should be accompanied by a low embodied energy and a long lifetime.[26] Given the fact that the processing window is broad in order to obtain efficient

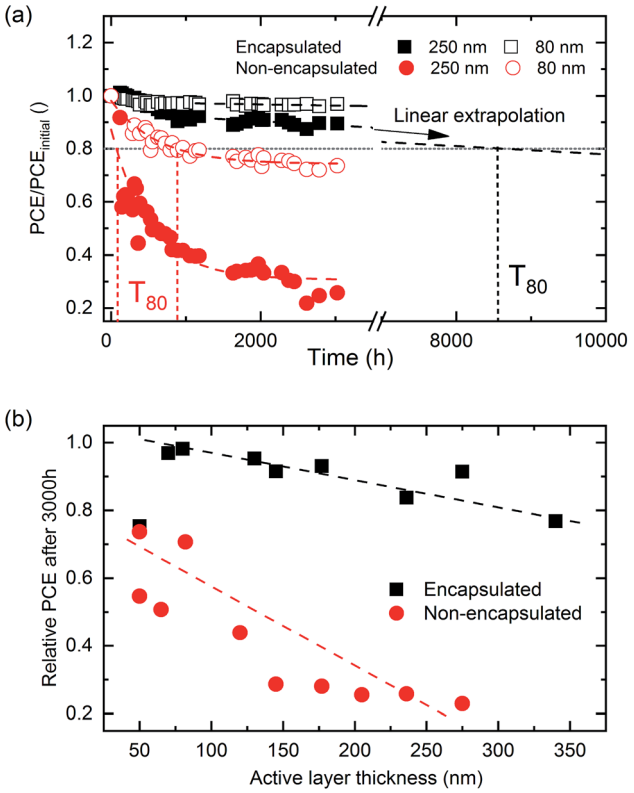


Fig. 6 Ageing test of P3HT:O-IDTBR solar cells stored in the dark with thinner and thicker photoactive layers and the effect of the encapsulation. (a) Normalized efficiency as a function of time for encapsulated (squares) and non-encapsulated (circles) devices. Dashed lines correspond to linear extrapolation. (b) Relative PCE *vs.* thickness of the photoactive layer study of encapsulated and non-encapsulated devices.

devices, we analysed whether the stability also exhibits a similar trend. Here, following the gradient approach, we tested the influence of photoactive layer thickness together with the effect of glass encapsulation on the long term stability of P3HT:O-IDTBR cells under ambient conditions. In particular, shelf lifetimes were evaluated by storing samples in the dark under ambient conditions between *JV* measurements following the requirements of ISOS-D-1.[51] Interestingly, the non-encapsulated samples enable observation of the accelerated degradation process of the devices, thus allowing us to assess the degradation scenario that encapsulated devices will suffer in a longer period of time (year scale).

The results show that the glass encapsulation has a very strong effect on stability (Fig. 6(a)), with encapsulated samples retaining more than 80% of the initial PCE after 3000 hours. The PCE of non-encapsulated devices, on the other hand, is reduced to values between 50% and 30% of their initial values after 3000 hours. The degradation in OPVs has been typically characterized by an initial burn-in stage followed by a linear behaviour.[52] The initial burn-in decay is clearly seen in the non-encapsulated devices (with no thickness dependence). The PCEs of non-encapsulated devices decrease exponentially after 1250 h, whilst the encapsulated devices exhibit an almost linear degradation over time. This indicates that the burn-in stage is related to external factors such as moisture and/or oxygen present in the device.[53,54] Fig. 6(a) also reveals that thicker photoactive layers of P3HT-O:IDTBR are consistently (for both encapsulated and non-encapsulated devices) more sensitive to degradation. This OPV degradation effect is mainly reflected by the decrease in the FF (Fig. S15†). Interestingly, the FF reduction is prominent for both encapsulated and non-encapsulated devices. This fact has been interpreted in the literature as interface degradation.[55] However, one may expect that interfacial effects will become more important in thinner films due to the relative weight of the interface with respect to the bulk in thinner films compared to thicker ones.

In order to understand the degradation mechanisms present in the P3HT:O-IDTBR system, we obtained co-local photocurrent images of both aged encapsulated and non-encapsulated devices (Fig. 7). The light-beam induced-current (LBIC) maps were measured under short circuit current conditions at different excitation wavelengths. Due to the complementary absorption of the photoactive materials, LBIC measured at 488 nm and 785 nm allows for selectively assessing the photocurrent contribution of P3HT and O-IDTBR, respectively. Photocurrent maps were also collected using illumination from the white light of a standard microscope lamp to understand the overall effect of white light on device degradation. These experiments are herein referred to as WhiteBIC.

First, we can observe that there is a significant difference in the magnitude of LBIC maps for the encapsulated and non-encapsulated devices (also supported by data in Table 2) in agreement with the solar cell data. Moreover, the encapsulated device shows a homogeneously distributed photocurrent map for all the excitation sources. On the other hand, the non-encapsulated counterpart exhibits a more heterogeneous distribution depending on the excitation wavelength. A second conclusion is that the degradation does not seem to occur at the same pace in P3HT and in O-IDTBR. This is depicted in the photocurrent histogram of the non-encapsulated devices, which reveals a parabolic distribution of LBIC at 488 nm and a bimodal distribution obtained at 785 nm excitation. These photocurrent maps suggest that P3HT suffers from a lower degradation rate compared to O-IDTBR. Thus, it is likely that the key factor of degradation is related to O-IDTBR.

White-light photocurrent maps confirm the convolution of the two effects by also showing bimodal photocurrent distribution. The bimodal distribution of both LBIC at 785 nm and WhiteBIC (O-IDTBR contribution) is explained as the sum of two factors: oxygen diffusion from the edges and the presence of pinholes in the electrode. Oxygen diffusion is more pronounced at the edges of the pixel, which accordingly exhibit less photocurrent compared to the central part of the device. The second mechanism explains the dark spots on the WhiteBIC photocurrent map as the presence of pinholes in the photoactive area.[56] Through these pinholes in the electrode, oxidizing agents such as oxygen and water can ingress into the device and react with $MoO_3$ and eventually propagate into the active layer. It is worth mentioning that pinholes were only found in the

 

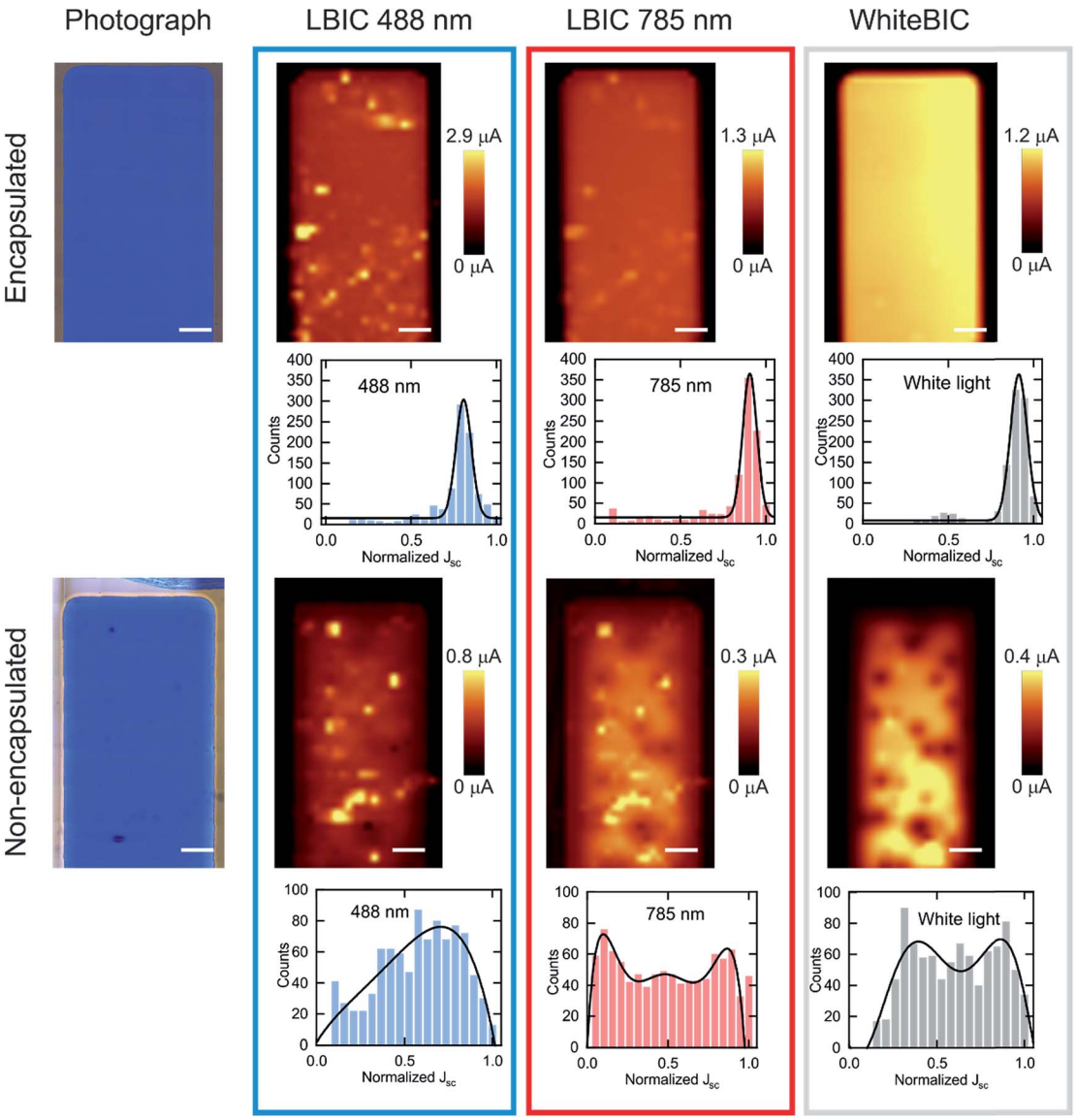


Fig. 7 Comparison of encapsulated (top) and non-encapsulated (bottom) thin P3HT:O-IDTBR devices. Optical images and light-beam induced-current (LBIC) maps measured at 488 nm and 785 nm and with white light (WhiteBIC) (from left to right). The scale bar corresponds to 500 μm. Normalized statistical histograms are given under each photocurrent map.

non-encapsulated devices; however these two degradation effects might appear in the encapsulated devices over time.

On the other hand, we carried out a similar study based on selective excitation to obtain photocurrent maps for thin and thick encapsulated devices (Fig S16†). The wider photocurrent distribution for thicker devices compared to the thinner ones suggests that the faster degradation observed in the thicker devices might be due to a larger amount of O-IDTBR in the photoactive layer or different morphologies depending on the thickness of the active layer. Finally, to verify that the degradation in thick films of P3HT:O-IDTBR blends evolves faster than in thinner films, wavelength-dependent measurements were carried out on non-encapsulated films (Fig. S17†). EQE spectra confirm that thicker P3HT:O-IDTBR devices clearly degrade faster than thinner ones. While the O-IDTBR contribution of the fresh, thick device is higher than that of the P3HT, in the degradation scenario the EQE shows clear degradation of O-IDTBR compared to P3HT, which is in agreement with the LBIC data. The reasons for the degradation of thinner films, in contrast to thicker films, are not fully clear since the EQE spectra of both fresh and aged devices maintain the same spectral shape, thus suggesting that homogeneous degradation of both materials takes place in encapsulated devices. Further degradation studies are required to fully explain the thickness dependent degradation; however, these studies are out of the scope of this work.

The relative PCE values are useful to compare the degradation rates for different thicknesses (Fig. 6(a)). However, the absolute PCE values obtained for encapsulated devices (Fig. S15†) reveal that, despite thinner devices (80 nm) being

Table 2 Photovoltaic parameters of P3HT:O-IDTBR fresh and degraded solar cells as a function of the encapsulation and thickness of the photoactive layer

| Encapsulated | Time | Photoactive layer thickness (nm) | $V_{oc}$ (V) | $J_{sc}$ (mA cm$^{-2}$) | FF (%) | PCE (%) | $PCE_{3000h}/PCE_{initial}$ | $T_{80}$ (h) |
|---|---|---|---|---|---|---|---|---|
| No | Fresh | 250 | 0.72 | −12.5 | 57.7 | 5.2 | 0.15 | 120 |
| | After 3000 h | | 0.42 | −5.8 | 32.7 | 0.8 | | |
| | Fresh | 80 | 0.69 | −8.9 | 56.9 | 3.5 | 0.6 | 700 |
| | After 3000 h | | 0.58 | −7.8 | 46.5 | 2.1 | | |
| Yes | Fresh | 250 | 0.70 | −13.1 | 47.3 | 4.32 | 0.83 | 8300[a] |
| | After 3000 h | | 0.68 | −12.7 | 41.6 | 3.6 | | |
| | Fresh | 80 | 0.70 | −8.9 | 55.8 | 3.5 | 0.97 | >5 years[a] |
| | After 3000 h | | 0.69 | −8.7 | 55.5 | 3.4 | | |

[a] Values calculated from estimated linear degradation.

more stable than thicker ones (250 nm), after 3000 hours the latter still outperform the former. This finding suggests that for long-term stability studies the absolute PCE values are as important as the degradation rate in order to draw a solid conclusion. Additionally, from Fig. 6(a) we can also obtain relevant information about the degradation of the devices such as the $T_{80}$ parameter. The $T_{80}$ is defined as the time required to achieve 80% of the initial performance. This stability parameter is a good estimation of how rapidly a solar cell degrades. Clearly, Table 2 shows that for non-encapsulated devices $T_{80}$ is larger for thinner (700 h) than for thicker devices (120 h).

In the case of the encapsulated counterpart, 3000 hours were not enough to achieve 80% of the initial value, and thus, an estimated linear degradation rate was assumed to calculate the corresponding $T_{80}$. According to the extrapolation, 8500 hours and more than 5 years would be required to yield 80% of the initial PCE for thicker and thinner devices, respectively. Interestingly, thinner devices overcome the absolute produced power of thicker devices after 25 000 working hours, providing 13% more energy. Fig. 6(b) shows the comparison of the relative PCE after 3000 hours and its dependence on the thickness of the photoactive layer for P3HT:O-IDTBR solar cells. For both encapsulated and non-encapsulated cells, thinner photoactive layers degrade more slowly. Correspondingly, after 3000 hours, thinner devices retain more PCE than thicker devices. We can conclude that, after evaluating several photoactive layer thicknesses of P3HT:O-IDTBR solar cells, thinner devices are more stable than thicker ones. This means that the studied system not only takes longer to achieve 80% of the initial performance but also requires less material to be manufactured. P3HT:O-IDTBR solar cells with a thinner photoactive layer combine the mentioned advantage of longer $T_{80}$ time with less employed material, a factor which makes them economically more convenient. Additionally, the degradation effect is more pronounced in O-IDTBR than in P3HT for thick films, albeit for thin films the degradation rates of both materials are similar.

## Conclusions

High throughput approaches have been used to screen solar cells based on P3HT and novel non-fullerene acceptors (NFAs). In particular, we have evaluated five commercially available acceptors including NFAs (ITIC, ITIC-M, O-IDTBR, EH-IDTBR and O-IDFBR) and $PC_{60}BM$ and ICBA as fullerene references. The analysis of variance (ANOVA) allowed for ranking the sensitivity of the studied parameters of P3HT based devices. We have found that the most influential parameters are, in decreasing order: (1) acceptor material; (2) choice of solvent system; (3) annealing temperature; (4) casting temperature; and (5) active layer thickness. A meta-study of more than one thousand P3HT based samples yielded two main conclusions. Firstly, the most promising P3HT:NFA system is that based on O-IDTBR. Secondly, the processing solvent system (CB:DCB) systematically results in higher efficiency for all blade coated P3HT:NFA solar cells. We have found that this better performance is related to appropriate vertical phase separation of the components of the photoactive layer, as well as to a reduction of the surface roughness together with an optimized morphology.

We have used a high throughput methodology based on thickness and annealing temperature gradients to further investigate the P3HT:O-IDTBR binary system. We have found that the post-annealing temperature is a more critical parameter than the deposition temperature, 120 °C being the optimum temperature. Moreover, we obtained power conversion efficiencies above 5% for this system over a broad photoactive layer thickness range. Finally, encapsulated and thinner P3HT:O-IDTBR devices (photoactive layer around 80–100 nm) also showed great potential in terms of stability according to their $T_{80}$ parameters, retaining more than 95% of the initial PCE after 3000 hours. Interestingly, we found that O-IDTBR is responsible for faster degradation in P3HT:O-IDTBR devices.

## Conflicts of interest

There are no conflicts to declare.

## Acknowledgements

This work was supported by the Spanish Ministerio de Economía y Competitividad (MINECO) under Grants MAT2015-70850-P, PGC2018-095411-B-I00 and SEV-2015-0496 in the framework of the Spanish Severo Ochoa Centre of Excellence, the EURECAT

Technology Centre, European Research Council through project ERC CoG648901 and H2020 Marie Curie actions through the SEPOMO project (Grant number 722651). We are also very thankful to Mr Fernando Gallegos for manufacturing the metallic holder, Mr Martí Gibert for the useful multiplexer/switcher design, Dr Bernhard Dörling for designing the doctor blade controller, Mr Adrián Francisco for helping with Raman fittings and Dr Marta Riba, Mrs Marta Gerbolés, Mrs Anna Crespí and Mr Andrés Gómez for helping with contact angle, XRD and AFM measurements, respectively. We acknowledge support of the publication fee by the CSIC Open Access Publication Support Initiative through its Unit of Information Resources for Research (URICI).

## Notes and references

1 J. Hou, O. Inganas, R. H. Friend and F. Gao, *Nat. Mater.*, 2018, **17**, 119–128.
2 N. Li, I. McCulloch and C. J. Brabec, *Energy Environ. Sci.*, 2018, **11**, 1355–1361.
3 J. Yuan, Y. Xu, G. Shi, X. Ling, L. Ying, F. Huang, T. H. Lee, H. Y. Woo, J. Y. Kim, Y. Cao and W. Ma, *J. Mater. Chem. A*, 2018, **6**, 10421–10432.
4 Y. Xu, J. Yuan, S. Zhou, M. Seifrid, L. Ying, B. Li, F. Huang, G. C. Bazan and W. Ma, *Adv. Funct. Mater.*, 2019, **29**, 1806747.
5 J. Yuan, M. J. Ford, Y. Xu, Y. Zhang, G. C. Bazan and W. Ma, *Adv. Energy Mater.*, 2018, **8**, 1703291.
6 S. Zhang, Y. Qin, J. Zhu and J. Hou, *Adv. Mater.*, 2018, **30**, e1800868.
7 J. Yuan, Y. Zhang, L. Zhou, G. Zhang, H.-L. Yip, T.-K. Lau, X. Lu, C. Zhu, H. Peng, P. A. Johnson, M. Leclerc, Y. Cao, J. Ulanski, Y. Li and Y. Zou, *Joule*, 2019, **3**, 1140–1151.
8 L. Meng, Y. Zhang, X. Wan, C. Li, X. Zhang, Y. Wang, X. Ke, Z. Xiao, L. Ding, R. Xia, H.-L. Yip, Y. Cao and Y. Chen, *Science*, 2018, **361**, 1094–1098.
9 E. Pascual-San José, A. Sánchez-Díaz, M. Stella, E. Martínez-Ferrero, M. I. Alonso and M. Campoy-Quiles, *Sci. Technol. Adv. Mater.*, 2018, **19**, 823–835.
10 A. Wadsworth, M. Moser, A. Marks, M. S. Little, N. Gasparini, C. J. Brabec, D. Baran and I. McCulloch, *Chem. Soc. Rev.*, 2019, **48**, 1596–1625.
11 A. T. Kleinschmidt, S. E. Root and D. J. Lipomi, *J. Mater. Chem. A*, 2017, **5**, 11396–11400.
12 N. V. Handa, A. V. Serrano, M. J. Robb and C. J. Hawker, *J. Polym. Sci., Part A: Polym. Chem.*, 2015, **53**, 831–841.
13 *Solaris Chem Inc*, http://www.solarischem.com/P3HT.html, accessed 15/02/2019, 2019.
14 R. Po, A. Bernardi, A. Calabrese, C. Carbonera, G. Corso and A. Pellegrino, *Energy Environ. Sci.*, 2014, **7**, 925.
15 H. Seyler, J. Subbiah, D. J. Jones, A. B. Holmes and W. W. Wong, *Beilstein J. Org. Chem.*, 2013, **9**, 1492–1500.
16 D. Chi, S. Qu, Z. Wang and J. Wang, *J. Mater. Chem. C*, 2014, **2**, 4383.
17 G. Zhao, Y. He and Y. Li, *Adv. Mater.*, 2010, **22**, 4355–4358.
18 I. Burgués-Ceballos, M. Stella, P. Lacharmoise and E. Martínez-Ferrero, *J. Mater. Chem. A*, 2014, **2**, 17711–17722.
19 S. Holliday, R. S. Ashraf, A. Wadsworth, D. Baran, S. A. Yousaf, C. B. Nielsen, C. H. Tan, S. D. Dimitrov, Z. Shang, N. Gasparini, M. Alamoudi, F. Laquai, C. J. Brabec, A. Salleo, J. R. Durrant and I. McCulloch, *Nat. Commun.*, 2016, **7**, 11585.
20 N. Gasparini, M. Salvador, T. Heumueller, M. Richter, A. Classen, S. Shrestha, G. J. Matt, S. Holliday, S. Strohm, H.-J. Egelhaaf, A. Wadsworth, D. Baran, I. McCulloch and C. J. Brabec, *Adv. Energy Mater.*, 2017, **7**, 1701561.
21 R.-Z. Liang, M. Babics, V. Savikhin, W. Zhang, V. M. Le Corre, S. Lopatin, Z. Kan, Y. Firdaus, S. Liu, I. McCulloch, M. F. Toney and P. M. Beaujuge, *Adv. Energy Mater.*, 2018, **8**, 1800264.
22 C.-H. Tan, A. Wadsworth, N. Gasparini, S. Wheeler, S. Holliday, R. S. Ashraf, S. D. Dimitrov, D. Baran, I. McCulloch and J. R. Durrant, *J. Phys. Chem. C*, 2019, **123**(10), 5826–5832.
23 B. Sanchez-Lengeling, L. M. Roch, J. D. Perea, S. Langner, C. J. Brabec and A. Aspuru-Guzik, *Adv. Theory Simul.*, 2019, **2**, 1800069.
24 A. Wadsworth, Z. Hamid, M. Bidwell, R. S. Ashraf, J. I. Khan, D. H. Anjum, C. Cendra, J. Yan, E. Rezasoltani, A. A. Y. Guilbert, M. Azzouzi, N. Gasparini, J. H. Bannock, D. Baran, H. Wu, J. C. de Mello, C. J. Brabec, A. Salleo, J. Nelson, F. Laquai and I. McCulloch, *Adv. Energy Mater.*, 2018, **8**, 1801001.
25 N. Gasparini, A. Gregori, M. Salvador, M. Biele, A. Wadsworth, S. Tedde, D. Baran, I. McCulloch and C. J. Brabec, *Adv. Mater. Technol.*, 2018, **3**, 1800104.
26 D. Baran, R. S. Ashraf, D. A. Hanifi, M. Abdelsamie, N. Gasparini, J. A. Rohr, S. Holliday, A. Wadsworth, S. Lockett, M. Neophytou, C. J. Emmott, J. Nelson, C. J. Brabec, A. Amassian, A. Salleo, T. Kirchartz, J. R. Durrant and I. McCulloch, *Nat. Mater.*, 2017, **16**, 363–369.
27 S. Chen, Y. Liu, L. Zhang, P. C. Y. Chow, Z. Wang, G. Zhang, W. Ma and H. Yan, *J. Am. Chem. Soc.*, 2017, **139**, 6298–6301.
28 B. Xiao, A. Tang, J. Yang, Z. Wei and E. Zhou, *ACS Macro Lett.*, 2017, **6**, 410–414.
29 B. Xiao, A. Tang, L. Cheng, J. Zhang, Z. Wei, Q. Zeng and E. Zhou, *Sol. RRL*, 2017, **1**, 1700166.
30 N. A. Mica, S. A. J. Thomson and I. D. W. Samuel, *Org. Electron.*, 2018, **63**, 415–420.
31 Y. Qin, M. A. Uddin, Y. Chen, B. Jang, K. Zhao, Z. Zheng, R. Yu, T. J. Shin, H. Y. Woo and J. Hou, *Adv. Mater.*, 2016, **28**, 9416–9422.
32 S. Strohm, F. Machui, S. Langner, P. Kubis, N. Gasparini, M. Salvador, I. McCulloch, H. J. Egelhaaf and C. J. Brabec, *Energy Environ. Sci.*, 2018, **11**, 2225–2234.
33 B. S. S. Pokuri, J. Sit, O. Wodo, D. Baran, T. Ameri, C. J. Brabec, A. J. Moule and B. Ganapathysubramanian, *Adv. Energy Mater.*, 2017, **7**, 1701269.
34 G. Ji, W. Zhao, J. Wei, L. Yan, Y. Han, Q. Luo, S. Yang, J. Hou and C.-Q. Ma, *J. Mater. Chem. A*, 2019, **7**, 212–220.
35 A. Sánchez-Díaz, X. Rodríguez-Martínez, L. Córcoles-Guija, G. Mora-Martín and M. Campoy-Quiles, *Adv. Electron. Mater.*, 2018, **4**, 1700477.

36 F. Nickel, C. Sprau, M. F. G. Klein, P. Kapetana, N. Christ, X. Liu, S. Klinkhammer, U. Lemmer and A. Colsmann, *Sol. Energy Mater. Sol. Cells*, 2012, **104**, 18–22.
37 M. Wojdyr, *J. Appl. Crystallogr.*, 2010, **43**, 1126–1128.
38 Y. J. Kim, K. H. Park, J. J. Ha, D. S. Chung, Y. H. Kim and C. E. Park, *Phys. Chem. Chem. Phys.*, 2014, **16**, 19874–19883.
39 S. Li, L. Ye, W. Zhao, S. Zhang, S. Mukherjee, H. Ade and J. Hou, *Adv. Mater.*, 2016, **28**, 9423–9429.
40 M. Azzouzi, J. Yan, T. Kirchartz, K. Liu, J. Wang, H. Wu and J. Nelson, *Phys. Rev. X*, 2018, **8**, 031055.
41 C. McDowell, M. Abdelsamie, M. F. Toney and G. C. Bazan, *Adv. Mater.*, 2018, e1707114, DOI: 10.1002/adma.201707114.
42 G. E. B. Archer, A. Saltelli and I. M. Sobol, *Journal of Statistical Computation and Simulation*, 1997, **58**, 99–120.
43 Y. Xie, W. Zhou, J. Yin, X. Hu, L. Zhang, X. Meng, Q. Ai and Y. Chen, *J. Mater. Chem. A*, 2016, **4**, 6158–6166.
44 D. Kekuda, H.-S. Lin, M. Chyi Wu, J.-S. Huang, K.-C. Ho and C.-W. Chu, *Sol. Energy Mater. Sol. Cells*, 2011, **95**, 419–422.
45 G.-H. Lim, J.-M. Zhuo, L.-Y. Wong, S.-J. Chua, L.-L. Chua and P. K. H. Ho, *Org. Electron.*, 2014, **15**, 449–460.
46 W. C. Tsoi, D. T. James, J. S. Kim, P. G. Nicholson, C. E. Murphy, D. D. Bradley, J. Nelson and J. S. Kim, *J. Am. Chem. Soc.*, 2011, **133**, 9834–9843.
47 S. K. Hau, H.-L. Yip, O. Acton, N. S. Baek, H. Ma and A. K. Y. Jen, *J. Mater. Chem.*, 2008, **18**, 5113.
48 L. Quan, R. G. Pablo, M. P. Paola, C. Silvia, T. Johann and M. Jordi, *Adv. Energy Mater.*, 2017, **7**, 1700356.
49 M. Campoy-Quiles, T. Ferenczi, T. Agostinelli, P. G. Etchegoin, Y. Kim, T. D. Anthopoulos, P. N. Stavrinou, D. D. Bradley and J. Nelson, *Nat. Mater.*, 2008, **7**, 158–164.
50 M. Campoy-Quiles, M. I. Alonso, D. D. C. Bradley and L. J. Richter, *Adv. Funct. Mater.*, 2014, **24**, 2116–2134.
51 M. O. Reese, S. A. Gevorgyan, M. Jørgensen, E. Bundgaard, S. R. Kurtz, D. S. Ginley, D. C. Olson, M. T. Lloyd, P. Morvillo, E. A. Katz, A. Elschner, O. Haillant, T. R. Currier, V. Shrotriya, M. Hermenau, M. Riede, K. R. Kirov, G. Trimmel, T. Rath, O. Inganäs, F. Zhang, M. Andersson, K. Tvingstedt, M. Lira-Cantu, D. Laird, C. McGuiness, S. Gowrisanker, M. Pannone, M. Xiao, J. Hauch, R. Steim, D. M. DeLongchamp, R. Rösch, H. Hoppe, N. Espinosa, A. Urbina, G. Yaman-Uzunoglu, J.-B. Bonekamp, A. J. J. M. van Breemen, C. Girotto, E. Voroshazi and F. C. Krebs, *Sol. Energy Mater. Sol. Cells*, 2011, **95**, 1253–1267.
52 C. H. Peters, I. T. Sachs-Quintana, W. R. Mateker, T. Heumueller, J. Rivnay, R. Noriega, Z. M. Beiley, E. T. Hoke, A. Salleo and M. D. McGehee, *Adv. Mater.*, 2012, **24**, 663–668.
53 N. Grossiord, J. M. Kroon, R. Andriessen and P. W. M. Blom, *Org. Electron.*, 2012, **13**, 432–456.
54 W. R. Mateker and M. D. McGehee, *Adv. Mater.*, 2017, **29**, 1603940.
55 E. Voroshazi, B. Verreet, T. Aernouts and P. Heremans, *Sol. Energy Mater. Sol. Cells*, 2011, **95**, 1303–1307.
56 R. Rösch, D. M. Tanenbaum, M. Jørgensen, M. Seeland, M. Bärenklau, M. Hermenau, E. Voroshazi, M. T. Lloyd, Y. Galagan, B. Zimmermann, U. Würfel, M. Hösel, H. F. Dam, S. A. Gevorgyan, S. Kudret, W. Maes, L. Lutsen, D. Vanderzande, R. Andriessen, G. Teran-Escobar, M. Lira-Cantu, A. Rivaton, G. Y. Uzunoğlu, D. Germack, B. Andreasen, M. V. Madsen, K. Norrman, H. Hoppe and F. C. Krebs, *Energy Environ. Sci.*, 2012, **5**, 6521.